Acta Crystallographica Section D
Biological Crystallography
ISSN 0907-4449

Structural and functional analyses of a bacterial homologue of hormone-sensitive lipase from a metagenomic library

Tri Duc Ngo,[a]‡ Bum Han Ryu,[b]‡ Hansol Ju,[b] Eunjin Jang,[b] Kwangsoo Park,[a] Kyeong Kyu Kim[a]* and T. Doohun Kim[b]*

[a]Department of Molecular Cell Biology, Samsung Biomedical Research Institute, Sungkyunkwan University School of Medicine, Suwon 440-746, Republic of Korea, and [b]Department of Molecular Science and Technology, Graduate School of Interdisciplinary Programs, Ajou University, Suwon 443-749, Republic of Korea

‡ These authors contributed equally to this work.

Correspondence e-mail: kyeongkyu@skku.edu, doohunkim@ajou.ac.kr

Received 23 March 2013
Accepted 15 May 2013

PDB Reference: Est25, 4j7a

Intracellular mobilization of fatty acids from triacylglycerols in mammalian adipose tissues proceeds through a series of lipolytic reactions. Among the enzymes involved, hormone-sensitive lipase (HSL) is noteworthy for its central role in energy homeostasis and the pathogenic role played by its dysregulation. By virtue of its broad substrate specificity, HSL may also serve as an industrial biocatalyst. In a previous report, Est25, a bacterial homologue of HSL, was identified from a metagenomic library by functional screening. Here, the crystal structure of Est25 is reported at 1.49 Å resolution; it exhibits an α/β-hydrolase fold consisting of a central β-sheet enclosed by α-helices on both sides. The structural features of the cap domain, the substrate-binding pocket and the dimeric interface of Est25, together with biochemical and biophysical studies including native PAGE, mass spectrometry, dynamic light scattering, gel filtration and enzyme assays, could provide a basis for understanding the properties and regulation of hormone-sensitive lipase (HSL). The increased stability of cross-linked Est25 aggregates (CLEA-Est25) and their potential for extensive reuse support the application of this preparation as a biocatalyst in biotransformation processes.

1. Introduction

During nutrient deprivation or enhanced demand for energy, lipolysis releases fatty acids and glycerol from triacylglycerols stored primarily in adipocytes. In this metabolic process, hormone-sensitive lipase (HSL; EC 3.1.1.79) mediates the hydrolysis of triglycerides to diglycerides and of diglycerides to monoglycerides, whereas monoacylglycerol lipase (MGL; EC 3.1.1.23) catalyzes the breakdown of monoglycerides to glycerol and fatty acids (Lafontan & Langin, 2009; Holm, 2003). Its pivotal role in lipolysis has drawn attention to HSL as a potential pharmaceutical target, because fatty-acid levels influence the pathogenesis of type II diabetes, obesity and cardiovascular diseases (Cascio *et al.*, 2012; Karpe *et al.*, 2011).

The human HSL gene (hHSL) encodes a polypeptide of 775 amino acids (~84 kDa), whereas human MGL (hMGL) is composed of only 303 amino acids (~33 kDa). The deduced amino-acid sequence of hHSL is approximately 80% identical to those of corresponding proteins from other mammalian species. However, the lack of significant homology to any other mammalian protein indicates that this enzyme family is very distantly related to other lipases and esterases in mammals. Sequence analysis suggests that mammalian HSLs are composed of two distinct domains: the N-terminal and C-terminal domains (Holm, 2003; Osterlund, 2001). While the N-terminal domain interacts with other proteins such as adipocyte lipid-binding protein (ALBP), the C-terminal

domain exerts hydrolytic activity on lipid substrates. Interestingly, the C-terminal domain of mammalian HSL shares regions of sequence and conserved motifs with the bacterial lipolytic IV family (Arpigny & Jaeger, 1999). Therefore, biochemical studies of the lipolytic IV family enzymes may provide insight into the structure and function of HSL. Compared with the lipolytic IV family proteins, the C-terminal domain of HSL contains an additional domain of ∼150 amino acids, known as a regulatory module, which influences the intrinsic activity of HSL through serine phosphorylation and protein–lipid interactions. To date, high-resolution structures of mammalian HSL-family members have not been available owing to the size and complex organization of these proteins; however, structures have been reported of several bacterial lipolytic IV family members, including Sto-Est from *Sulfolobus tokodaii* (Angkawidjaja *et al.*, 2012); PestE from *Pyrobaculum calidifontis* (Palm *et al.*, 2011); EstE1 and EstE7 from metagenomic libraries (Byun *et al.*, 2007; Nam *et al.*, 2009); HerE from *Rhodococcus* sp. (Zhu *et al.*, 2003); AFEST from *Archaeoglobus fulgidus* (De Simone *et al.*, 2001); EST2 from *Alicyclobacillus acidocaldarius* (De Simone *et al.*, 2000) and BFAE from *Bacillus subtilis* (Wei *et al.*, 1999).

Interestingly, HSL-family proteins have a broader substrate specificity than other lipases and esterases (Manco *et al.*, 2012; Rodriguez *et al.*, 2010). Specifically, HSL can hydrolyze all types of acylglycerols, cholesteryl esters, retinyl esters, fatty-acid esters and steroids, as well as other lipid substrates. In contrast, MGL only hydrolyzes a select group of monoacylglycerols. The broad specificity of the HSL-family members increases the potential utility of these proteins as biocatalysts in environmental and industrial applications, in a similar way to the P450 cytochromes and glutathione *S*-transferases (Podust & Sherman, 2012; Chronopoulou & Labrou, 2009). In addition, the discovery of novel HSL-family enzymes using the metagenomic approach further expands the potential range of enzymatic functions to be applied.

In previous reports, a new bacterial homologue (Est25) of the HSL family was identified from an uncultured bacterium and was characterized as a member of the type IV lipolytic enzymes (Kim *et al.*, 2006, 2007). In this study, we analyzed the structure and function of Est25 in order to obtain a broader understanding of the HSL-family enzymes and to investigate the potential uses of Est25 as a biocatalyst.

2. Materials and methods

2.1. Bacterial strains, enzymes and reagents

The cloning and expression steps were performed using *Escherichia coli* XL1-Blue (Qiagen, California, USA). Enzyme substrates, antibiotics and LB broth were obtained from Sigma–Aldrich (Seoul, Republic of Korea). PD-10 and Ni–NTA columns were obtained from GE Healthcare Biosciences (Pennsylvania, USA). All other chemicals were of reagent grade and were obtained from other commercial sources.

2.2. Sequence analysis and phylogenetic tree

To identify related enzymes in the HSL family, the NCBI protein-sequence database was searched for sequences similar to the primary sequence of Est25 (GenBank ID DQ025532) using *PSI-BLAST* (Jones & Swindells, 2002). All of the amino-acid sequences were retrieved in FASTA format. Multiple sequence alignments were performed with *Clustal Omega* (Sievers *et al.*, 2011) and the results were rendered using *ESPript* (Gouet *et al.*, 2003). A phylogenetic tree was built using the *Molecular Evolutionary Genetics Analysis* (*MEGA*) software v.5.0 and the neighbour-joining method with 5000 iterations to calculate bootstrap confidence levels (Tamura *et al.*, 2011).

2.3. Expression, purification and characterization of Est25

The molecular cloning and purification of Est25 have been described previously (Kim *et al.*, 2006, 2007). In brief, transformed cells were grown in LB medium containing ampicillin (100 µg ml^{-1}) at 310 K and were induced with 1 m*M* isopropyl *β*-D-1-thiogalactopyranoside (IPTG). After 4 h, the cells were harvested, resuspended and sonicated in buffer *A* consisting of 50 m*M* sodium phosphate pH 8.0, 300 m*M* sodium chloride, 10 m*M* imidazole. After sonication, the crude cell extract was centrifuged at 15 000 rev min^{-1} for 20 min and the supernatant was loaded onto Ni–NTA resin and washed with 20 m*M* imidazole. The Est25 protein was then eluted in buffer *B* containing 250 m*M* imidazole with buffer *A* and desalted with phosphate-buffered saline (PBS) pH 7.4 using a PD-10 column. The purity of the Est25 protein was confirmed by SDS–PAGE and concentrations were determined using the Bio-Rad Protein Assay kit with bovine serum albumin (BSA) as a standard. The purified protein was concentrated to 10 mg ml^{-1} using an Amicon Ultrapure-15 centrifugal filter (Millipore, Massachusetts, USA). Selenomethionyl (SeMet) protein was purified using the same method as that used for the native Est25. The purified native and SeMet Est25 proteins with a His tag at the N-terminus were used for crystallization without further cleavage.

For activity staining, native PAGE was performed using a discontinuous gel system with a 4% stacking gel and an 8% resolving gel. The gels were rinsed three times with distilled water and the separating gel was soaked in 20 m*M* Tris–HCl pH 8.0 containing 10 µ*M* 4-methylumbelliferyl (4-MU) acetate for 5 min at 295 K. The fluorescence of 4-methylumbelliferone was visually detected in a UV-incubation box (Intron Biotechnologies, Seoul, Republic of Korea). Matrix-assisted laser desorption/ionization time-of-flight mass spectrometry (MALDI-TOF MS) was performed in the positive-ion mode using a Voyager DE STR system (Applied Biosystems, National Collaborative Inter-University Research Facilities, Seoul, Republic of Korea). Dynamic light-scattering (DLS) profiles were measured using a Zetasizer Nano S system (Malvern Instruments, Malvern, England). Est25 preparations were passed through a 0.1 µm filter before dilution and were allowed to equilibrate to 293 K prior to DLS measurements at the same temperature. Multiple data-set replicates were

Table 1
Data-collection and refinement statistics for Est25.

Values in parentheses are for the last resolution shell.

		SeMet derivative		
	Native	Peak	Inflection	Remote
Data collection				
Space group	*C*2	*C*2		
Unit-cell parameters (Å, °)	*a* = 197.76, *b* = 95.21, *c* = 99.42, $\alpha = \gamma = 90$, $\beta = 97.05$	*a* = 198.87, *b* = 95.27, *c* = 99.27, $\alpha = \gamma = 90$, $\beta = 97.38$		
Molecules in asymmetric unit	4	4		
Wavelength (Å)	1.0000	0.9789	0.9792	0.9640
Resolution (Å)	50.00–1.49	50.00–2.02	50.00–2.02	50.00–2.02
R_{sym} or R_{merge}† (%)	5.0 (31.6)	8.9 (29.6)	8.7 (29.9)	7.8 (26.8)
Mean $I/\sigma(I)$	27.83 (3.6)	16.59 (3.6)	16.50 (3.5)	17.06 (3.8)
Completeness (%)	96.2 (90.1)	99.5 (99.9)	99.6 (100)	99.6 (100)
Multiplicity	3.5 (3.3)	3.8 (3.6)	3.8 (3.6)	3.8 (3.6)
Refinement				
Resolution (Å)	28.55–1.49			
No. of reflections	285892			
R_{work}‡/R_{free}§ (%)	14.34/16.95			
No. of atoms				
Protein	10560			
Ligand/ion	—			
Water	2111			
R.m.s.d.¶				
Bond lengths (Å)	0.006			
Bond angles (°)	1.18			
Ramachandran statistics†† (%)				
Favoured	97.0			
Allowed	3.0			
Disallowed	0.0			

† $R_{merge} = \sum_{hkl}\sum_i |I_i(hkl) - \langle I(hkl)\rangle| / \sum_{hkl}\sum_i I_i(hkl)$, where $I_i(hkl)$ is the the ith measurement of the intensity of reflection hkl and $\langle I(hkl)\rangle$ is the mean intensity of reflection hkl. ‡ $R_{cryst} = \sum_{hkl} ||F_{obs}| - |F_{calc}|| / \sum_{hkl} |F_{obs}|$, where F_{obs} is the observed structure factor and F_{calc} is the structure factor calculated from the model. § R_{free} is calculated in the same manner as R_{cryst} using 5% of all reflections, which were excluded from refinement. ¶ Root-mean-square deviation. †† Calculated by *MolProbity*.

analyzed using the *DTS* 5.10 software supplied by the manufacturer. The calculated hydrodynamic radius was corrected to standard solvent conditions.

2.4. Protein crystallization and data collection

Initial crystallization trials were performed at 295 K using the microbatch crystallization method (Chayen *et al.*, 1990) under a thin layer of Al's oil with the Index (Hampton Research, California, USA) and Wizard (Jena Bioscience, Germany) screening kits. Each drop was prepared by mixing 1 µl reservoir solution and 1 µl protein solution and the drop was then covered with oil using Nunc MiniTrays (Nalge Nunc International, New York, USA). Crystallization conditions for diffraction experiments were optimized by changing various parameters. Diffraction-quality crystals were obtained using 2.4 *M* sodium malonate pH 7.0 as the reservoir solution. Crystals were transferred into a cryosolvent consisting of 2.4 *M* sodium malonate pH 7.0, 30% glycerol before being flash-cooled in a cold nitrogen stream.

All diffraction data were collected on beamline NW12 at the Photon Factory, Tsukuba, Japan using an ADSC Quantum 210 detector. The native data were collected to 1.49 Å resolution at a wavelength of 1.0000 Å. MAD data were collected to 2.02 Å resolution from an SeMet-derivative crystal at three wavelengths (peak, 0.97888 Å; inflection, 0.97917 Å; high-energy remote, 0.96395 Å; Table 1). The peak and inflection-point wavelengths were determined by recording an X-ray fluorescence spectrum. The native and SeMet-derivative data were indexed, integrated and scaled using *HKL*-2000 (Otwinowski & Minor, 1997).

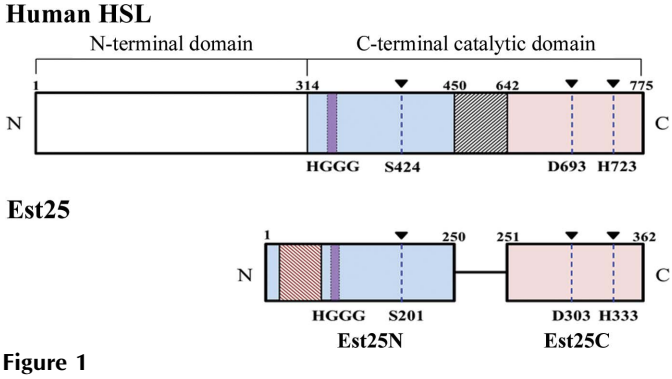

Figure 1
Structural organization of human HSL (hHSL) and Est25. hHSL is composed of an N-terminal domain and a C-terminal domain. Note that the C-terminal domain harbours the catalytic triad (Ser-Asp-His) and the conservative HGGG motif. Est25 is also divided into Est25N and Est25C with a regulatory module of hHSL as a boundary.

2.5. Structure determination and refinement

The structure of the SeMet-derivative protein was determined using the multi-wavelength anomalous diffraction (MAD) method. *SOLVE* (Terwilliger & Berendzen, 1999) and *RESOLVE* (Terwilliger, 2001) were used to locate and refine the selenium sites. Phases were calculated and used to produce a 2.02 Å resolution electron-density map. After phasing, density modification was performed using *RESOLVE*. Automated model building was performed using *ARP*/*wARP* (Langer *et al.*, 2008). The regions that were not automatically constructed were manually built using *Coot* (Emsley & Cowtan, 2004). The model was refined against the SeMet-derivative data using *REFMAC* (Murshudov *et al.*, 2011). The refined SeMet-derivative model was then used as an initial search model for molecular-replacement solution of the native data set using *MOLREP* (Vagin & Teplyakov, 2010). The model was refined over many steps using *REFMAC* and *PHENIX* (Adams *et al.*, 2010). The quality of the final model was evaluated with *PROCHECK* (Laskowski *et al.*, 1993). Structural features were visualized and analyzed using

PyMOL (Schrödinger). The coordinates and structural factors of Est25 have been deposited in the Protein Data Bank with accession code 4j7a.

2.6. Enzyme assays

The hydrolase activity of Est25 was determined by measuring the amount of *p*-nitrophenol released during hydrolysis at 405 nm using a VersaMax Bio-Rad 680 microplate reader (Kim *et al.*, 2012; Hwang *et al.*, 2010). The substrates containing *p*-nitrophenyl groups were *p*-nitrophenyl acetate (C_2; p-NA), *p*-nitrophenyl butyrate (C_4; p-NB), *p*-nitrophenyl octanoate (C_8; p-NO), *p*-nitrophenyl decanoate (C_{10}; p-NDe), *p*-nitrophenyl dodecanoate (C_{12}; p-NDo) and *p*-nitrophenyl phosphate (p-NP). The naphthyl-group derivatives 1-naphthyl acetate (1-NA), 2-naphthyl acetate (2-NA), 1-naphthyl butyrate (1-NB) and 1-naphthyl phosphate (1-NP) were also used. The standard assay solution contained 0.9 ml 0.3 m*M* substrate solution in 20 m*M* Tris–HCl pH 8.0 and 30 µg Est25 protein. The reaction mixture was incubated for 5 min and its absorbance was determined at 310 nm. For the hydrolysis of tertiary alcohol esters (TAEs), 100 µg Est25 was added to the substrate-mixture solutions containing phenol red (2 mg ml^{-1}) and 25 m*M* *t*-butyl acetate, linalyl acetate or α-terpinyl acetate in 20 m*M* Tris–HCl pH 8.0 buffer.

2.7. Cross-linked enzyme aggregate (CLEA) preparation

To prepare CLEAs, purified Est25 (500 µg) was precipitated with 80% ammonium sulfate in 25 m*M* Tris–HCl pH 8.0. Glutaraldehyde (final concentration 0.1 m*M*) was then added to cross-link the aggregates, followed by incubation for 12 h at room temperature with gentle agitation (Kim *et al.*, 2012; Taboada-Puig *et al.*, 2011). The suspension was centrifuged at 15 000*g* and 277 K for 10 min. The pellet (CLEAs) was resuspended and washed repeatedly until enzyme activity was no longer detected in the supernatant. The resulting CLEAs were resuspended and stored at 277 K for further use. The activities of free Est25 and CLEA-Est25 were determined by monitoring the hydrolysis of *p*-nitrophenyl acetate (C_2). The surface morphology of CLEA-Est25 was examined using a SUPRA 55VP (Carl Zeiss, New York, USA). Images were

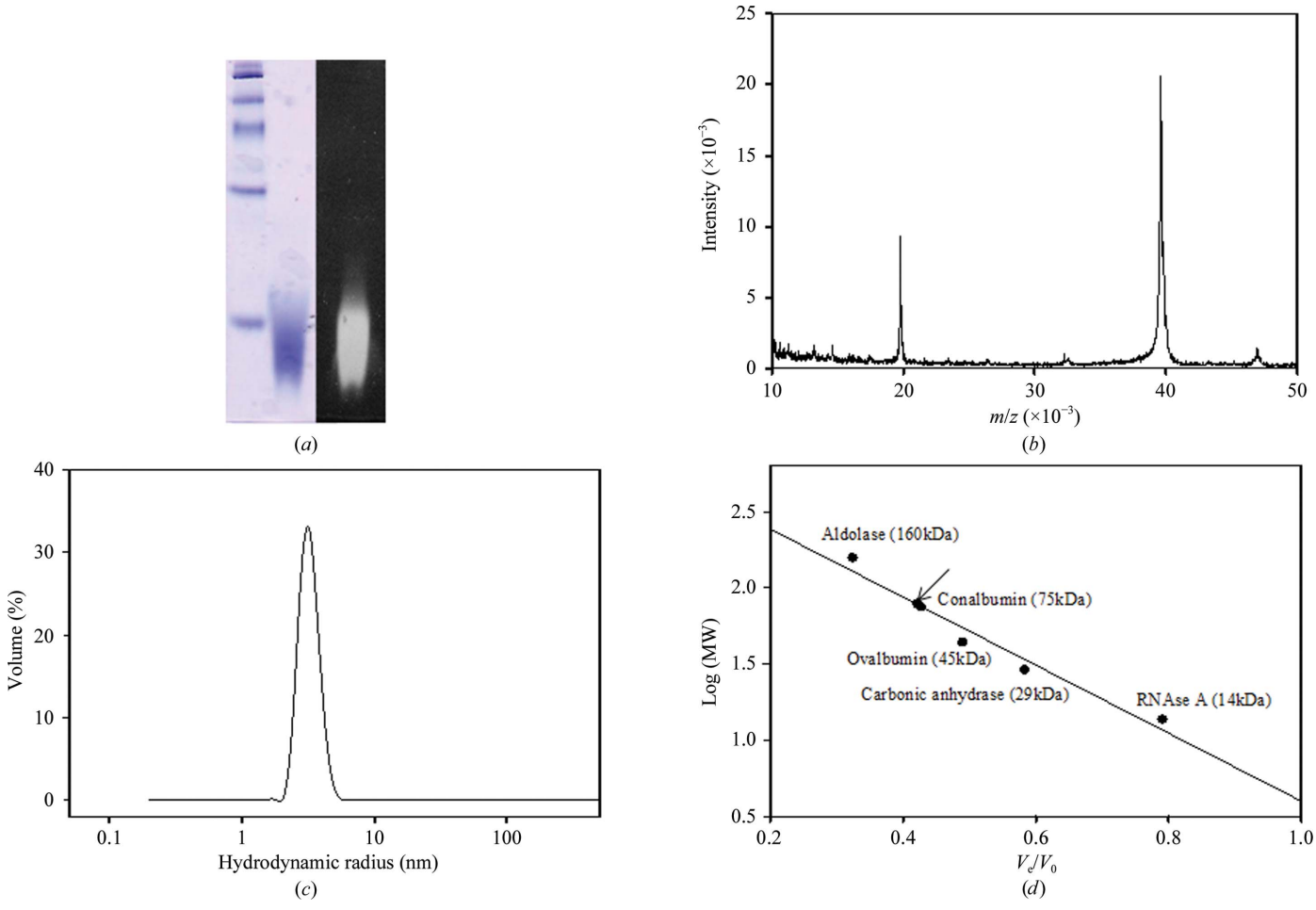

Figure 2
Overlay activity assay and molecular-weight analysis of Est25. (*a*) Native PAGE analysis was performed, followed by Coomassie staining (left). The gel was soaked in 4-MU acetate solution for 5 min and fluorescence was observed under UV light (right). (*b*) MALDI-TOF mass spectrum of Est25. The $[M + H]^+$ and $[M + 2H]^{2+}$ ion peaks were at *m*/*z* values of 39.8 and 19.7 kDa, respectively. (*c*) Dynamic light-scattering results for Est25. Note the single peak for Est25. (*d*) Size-exclusion chromatography of Est25 against standard marker proteins. (*c*) and (*d*) indicate that Est25 exists as a dimer in solution.

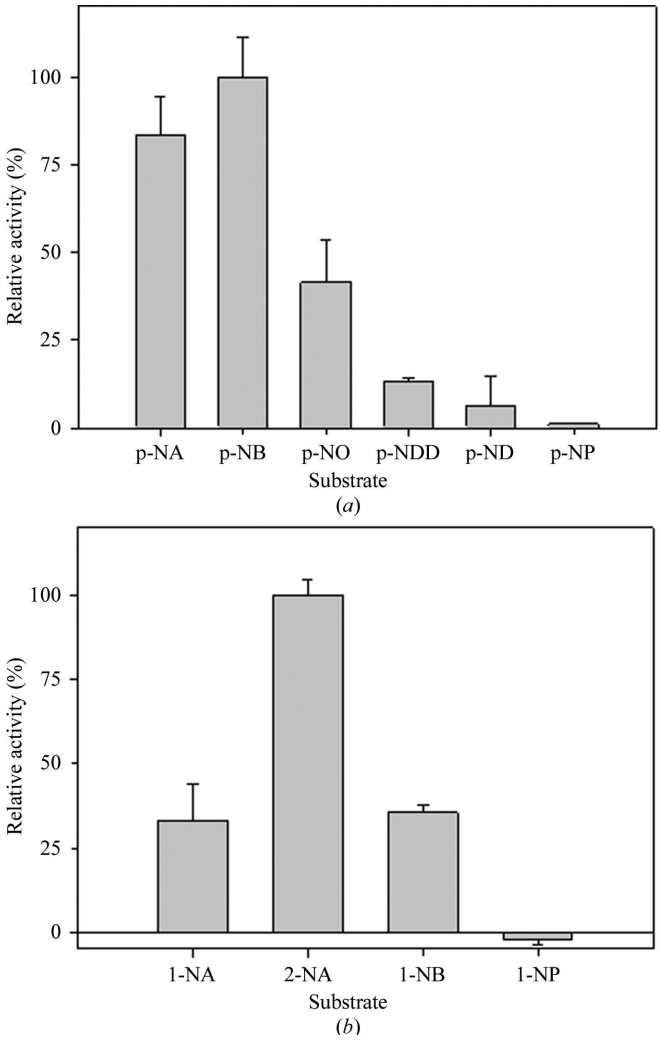

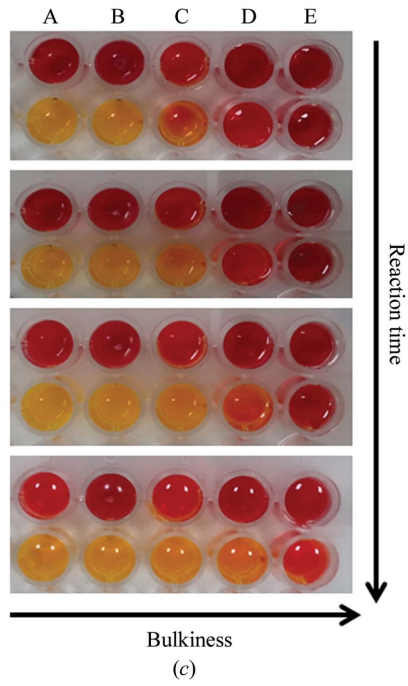

Figure 3
Substrate specificities, regiospecificities and tertiary alcohol ester-hydrolysis assay of Est25. (*a*) Substrate specificities of Est25 were determined using *p*-nitrophenyl esters of various chain lengths. (*b*) Regiospecificities of Est25 were determined for 1-naphthyl acetate, 2-naphthyl acetate, 1-naphthyl butyrate and 1-naphthyl phosphate. (*c*) The hydrolysis of tertiary alcohol esters (TAEs) by Est25 was measured using a pH-shift assay for acetate esters (A, *p*-nitrophenyl acetate; B, 1-naphthyl acetate; C, linalyl acetate; D, *tert*-butyl acetate; E, α-terpinyl acetate). The reaction times were 1, 5, 30 and 120 min from top to bottom. At each stage, the first and second rows included buffer and Est25, respectively.

taken at an accelerating voltage of 2 kV at various magnifications ranging from 10 000× to 200 000×. For chemical stability analysis, the effects of several chemical compounds on the enzymatic activities of CLEA-Est25 and free Est25 were determined. The enzymatic activity in the buffer-only condition was defined as 100%. Stabilities were determined by measuring the residual activity of the enzyme after 1 h incubation at 298 K. All experiments were repeated at least three times. For the reusability study, CLEA-Est25 was used for an additional nine cycles. After each cycle, the pellet was resuspended and washed repeatedly (usually three times) until enzyme activity was not detected in the supernatant.

3. Results and discussion

3.1. Phylogenetic and sequence analyses of Est25

Phylogenetic analysis was performed to clarify the evolutionary relationship of Est25 to bacterial lipolytic families. As shown in Supplementary Fig. S1[1], Est25 was clustered in a branch of the family IV group that shared 26.3 and 24.6% sequence identity with LipP from *Pseudomonas* sp. strain B11-1 (AAC38151) and EstA from *A. fulgidus* DSM 4304 (AAB89533), respectively. In contrast, Est25 shared ∼10% sequence identity with members of the neighbouring family VI and VII groups, including an esterase from *Spirulina platensis* (AAB30793), EstB from *P. fluorescens* (AAC60403), PnbA from *B. subtilis* (P37967) and a phenylcarbamate hydrolase from *Arthrobacter oxydans* P52 (Q01470). Sequence analysis using the Pfam protein databases identified an α/β-hydrolase fold (Pfam07859) that spans the full length of Est25. Est25 has a conserved catalytic triad Ser201–Asp303–His333 and the nucleophilic Ser201 is located in the characteristic Gly191-*X*-Ser201-*X*-Gly203 pentapeptide motif.

Est25 also showed sequence similarity to the C-terminal catalytic domain of hHSL, except for a region comprising a regulatory module (residues 450–642). We divided Est25 into two domains, Est25N (residues 1–250) and Est25C (residues 251–362), based on the location of the regulatory domain (Fig. 1). A significant degree of similarity between the primary sequences of the C-terminal domains of HSL and Est25 supports a common evolutionary origin of these proteins. The most essential residues for the structural framework and

[1] Supplementary material has been deposited in the IUCr electronic archive (Reference: MN5032). Services for accessing this material are described at the back of the journal.

catalytic activity are well conserved between mammalian HSL-family members and Est25. For example, a catalytic serine (Ser201) in Est25N and the other two catalytic residues (Asp303 and His333) in Est25C could be perfectly matched to corresponding residues in proteins within the HSL family. In addition, the ^{124}HGGG^{127} motif that contributes to the formation of the oxyanion hole in close proximity to the active site is also highly conserved among HSL members and Est25. In this sense, the structural and functional studies of Est25 may yield information that is relevant to the function and reaction mechanism of HSL.

3.2. Biochemical characterization of Est25

The recombinant Est25 was purified to near-homogeneity by affinity chromatography. As shown in Fig. 2(*a*), a single band representing Est25 was observed by native PAGE after Coomassie Brilliant Blue (CBB) staining. After purification, the hydrolytic activity of Est25 was determined by activity staining using 4-MU acetate as a substrate. High fluorescence owing to the formation of 4-methylumbelliferone was observed at the position corresponding to the protein on the zymogram. Mass-spectrometric analysis gave a major peak (*m*/*z*) at 39.6 kDa corresponding to the molecular weight of Est25 (Fig. 2*b*). The hydrodynamic radius (R_h) of Est25 was found to be 3.4 $\pm$ 0.2 nm based on DLS, indicating a uniform shape and dimeric state of Est25 (Fig. 2*c*). The molecular mass of Est25 was estimated to be 78.5 kDa from the elution profile of Est25 on size-exclusion chromatography (SEC), confirming that Est25 exists as a dimer in solution (Fig. 2*d*).

The substrate specificities of Est25 towards *p*-NP esters of various chain lengths and esters of naphthyl derivatives were analyzed in 25 m*M* Tris–HCl buffer pH 7.5 at 293 K (Figs. 3*a* and 3*b*). The substrates included *p*-NP esters of acetate (C_2), butyrate (C_4), octanoate (C_8), decanoate (C_{10}) and dodecanoate (C_{12}) at 1 m*M*. As shown in Fig. 3(*a*), Est25 showed a strong preference towards short-chain esters such as *p*-NA (C_2) or *p*-NB (C_4). In contrast, little activity was observed towards long-chain esters such as *p*-nitrophenyl dodecanoate (*p*-NDo; C_{12}). Specifically, the hydrolytic activity towards *p*-NDe (C_{10}) was only 12% of that measured towards *p*-NA (C_2). When naphthyl derivatives were used as substrates, the highest activities were obtained with 2-naphthyl acetate (2-NA) followed by 1-naphthyl acetate (1-NA) and 1-naphthyl butyrate (1-NB). However, Est25 was unable to hydrolyze *p*-nitrophenyl phosphate (*p*-NP) or 1-naphthyl phosphate (1-NP).

The GGG(A)*X* motif present in the oxyanion hole of the lipases and esterases has recently been proposed to be responsible for the ability of these enzymes to hydrolyze TAEs (Rehdorf *et al.*, 2012; Herter *et al.*, 2011). Taking into account the presence of a ^{124}HGGG^{127} motif in Est25, the ability of Est25 to hydrolyze TAEs was tested using *tert*-butyl acetate, linalyl acetate and α-terpinyl acetate as substrates. A pH-indicator-based colorimetric assay based upon the release of acetic acid was employed. As shown in Fig. 3(*c*), Est25

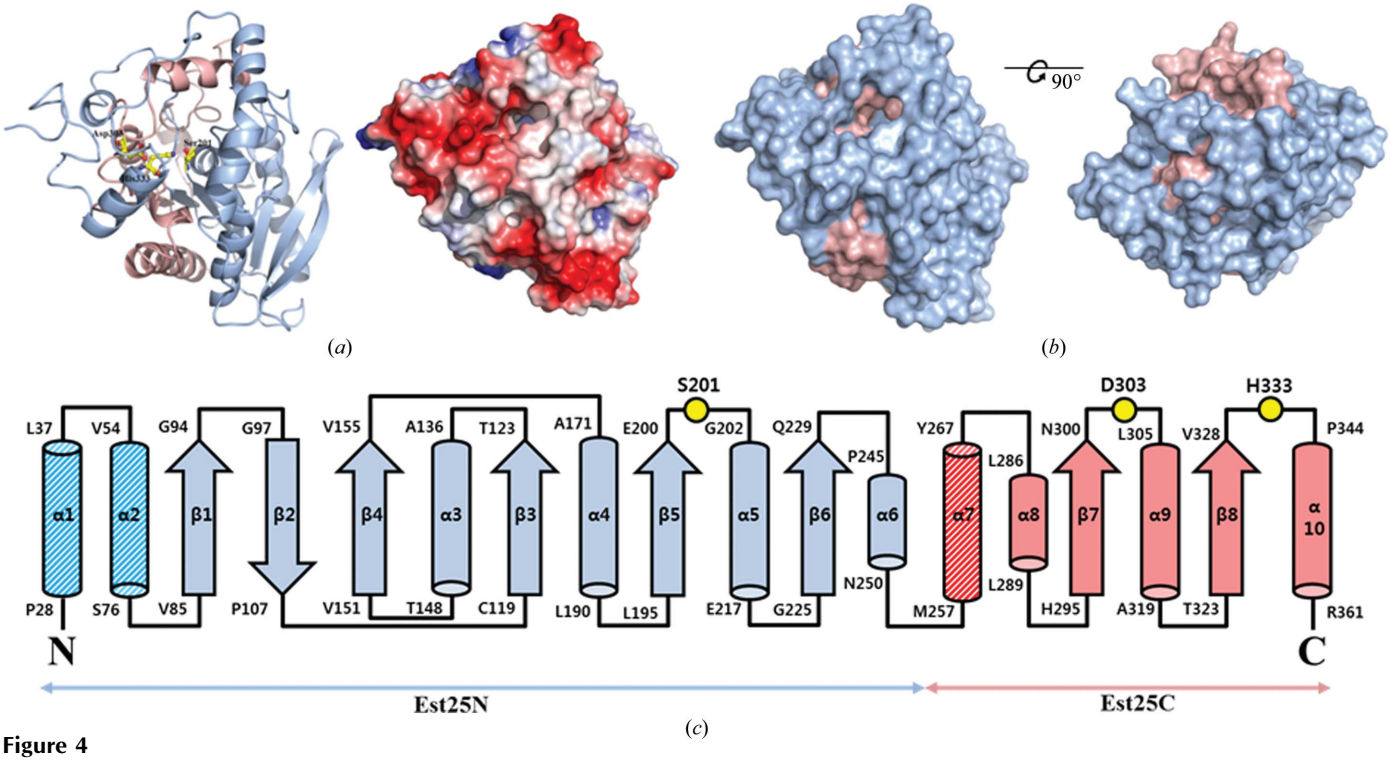

Figure 4
Structural visualization and topology diagram of Est25. Sky-blue and pink regions indicate the N-terminal (Est25N) and C-terminal (Est25C) domains of Est25, respectively. This colouring scheme is the same as that in Fig. 1. (*a*) Secondary structures (ribbon diagram) with catalytic triad residues (yellow; ball-and-stick representation) and the electrostatic potential of Est25 are shown. Blue and red represent positive and negative charge, respectively. (*b*) Surface representations of Est25 are shown from two viewpoints. (*c*) Topology diagram of Est25. The catalytic triad is shown as yellow spots. The starting and ending amino acids of each secondary structure are shown. Secondary structures for the cap region are shaded for comparison.

hydrolyzed *tert*-butyl acetate and linalyl acetate as well as the bulky substrate α-terpinyl acetate. The preparation of tertiary alcohols by enzymatic methods is a very important process because these alcohols are expensive building blocks for pharmaceuticals. Accordingly, Est25 holds promise for use as biocatalyst in pharmaceutical applications owing to its capacity to generate tertiary alcohols.

3.3. Overall structure of Est25

The 1.49 Å resolution crystal structure of Est25 was determined in space group *C*2 by multiple-wavelength anomalous dispersion (MAD) (Table 1). Several cycles of simulated-annealing, minimization and *B*-factor refinement using *PHENIX* and *REFMAC* followed by manual model rebuilding reduced the *R* values for all data in the resolution range 28.55–1.49 Å. The *R* factor of the present model was 14.34%, with an $R_{\rm free}$ of 16.95%. The crystallographic statistics for data collection and structure refinement are summarized in Table 1. The final structure of Est25 displayed a marginally ellipsoidal shape, with approximate dimensions of 60 × 56 × 48 Å (Fig. 4*a*). There were four subunits in the asymmetric unit, in which two dimers are arranged with polar angles of (113.7, −2.7, 172.8°) and a translation of (75.3, 97.0, 100.8 Å). Each dimer in the asymmetric unit is related by twofold noncrystallographic symmetry. The pairwise root-mean-square deviation (r.m.s.d.) between all atoms of the four molecules in the asymmetric unit was 0.19–0.35 Å. Calculation of the electrostatic potential showed that the molecular surfaces of Est25 were negatively charged. The first subunit (subunit *A*) was used for structural analysis unless otherwise specified.

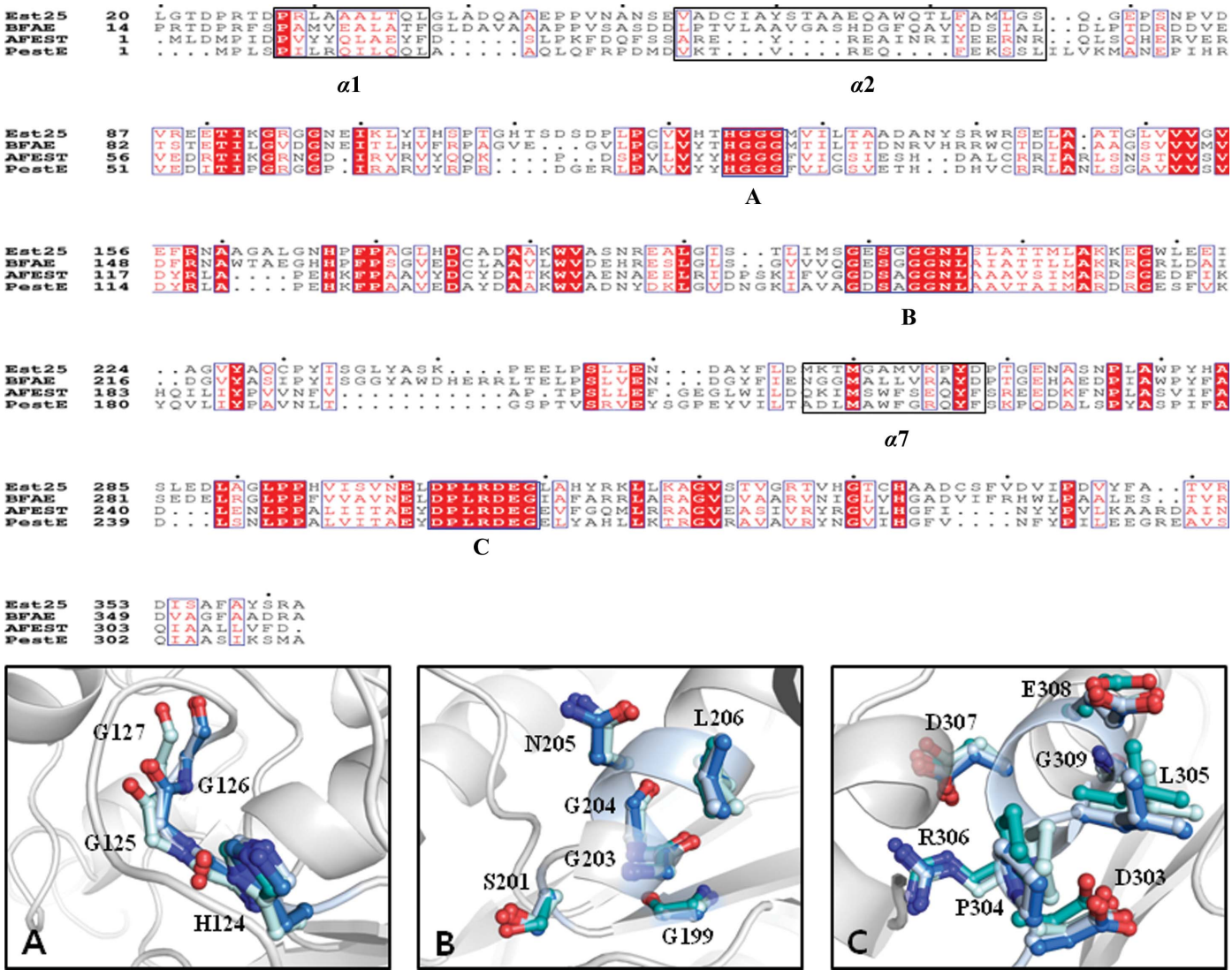

Figure 5
Multiple sequence alignment of Est25 and three structurally homologous enzymes (PDB entries 1jkm, brefeldin A esterase from *B. subtilis*; 1jji, hyperthermophilic carboxylesterase from *A. fulgidus*; 3zwq, hyperthermophilic esterase from *P. calidifontis*). Three helices (α1, α2 and α7) of the cap region are shown in the black boxes. Identical and highly conserved residues are shown in red and white, respectively. The three highly conserved motifs are indicated by the black boxes with labels (A, B and C) at the bottom. The residues in these conserved motifs of Est25 are indicated by ball-and-stick models and overlap with those of the three related enzymes. A, ^{124}HGGG^{127} motif; B, ^{199}G*X*S*X*GGNL^{206} motif; C, ^{303}DPLRDEG^{310} motif.

Est25 has a characteristic α/β-fold with a small cap domain composed of $\alpha1$ (Leu28–Pro37), $\alpha2$ (Val54–Met74) and $\alpha7$ (Met257–Tyr267). The α/β-hydrolase fold provides a stable scaffold for the active sites of a wide variety of enzymes, including lipases, proteases and esterases. The central α/β-fold of Est25 has a mixed β-sheet composed of eight β-strands (only strand $\beta2$ is antiparallel) surrounded by six helices, $\alpha3$ (Ala136–Thr148), $\alpha4$ (Ala171–Leu195), $\alpha5$ (Gly202–Glu217), $\alpha6$ (Pro245–Asn250), $\alpha8$ (Leu286–Leu289) and $\alpha9$ (Leu305–Ala319), that are packed on both sides of the β-sheet. Furthermore, the central β-sheet has a left-handed twist orientation, leading to an angle of approximately 125° between $\beta1$ and $\beta8$. Est25N is composed of six α-helices ($\alpha1$–$\alpha6$) and six β-strands ($\beta1$–$\beta6$), most of which are associated with the formation of the α/β-fold domain (Fig. 4*b*). In contrast, Est25C has four α-helices and two β-strands. The $\alpha7$ helix in Est25C is involved in cap formation with the $\alpha1$ and $\alpha2$ helices of Est25N, while two helices ($\alpha9$ and $\alpha10$) and one strand ($\beta8$) are involved in dimer formation (Supplementary Fig. S2). The small cap region, which is located on top of the substrate-binding pocket of Est25, seems to control substrate entry or recognition by maintaining the structural integrity around the binding pocket, because access of the substrate to the binding pocket is only possible through the cap domain.

Sequence alignment clearly indicated that the regulatory module in the C-terminal domain of hHSL is situated between the $\alpha6$ helix and the $\beta7$ strand. The α/β-hydrolase scaffold can accommodate a number of different insertions without disturbing the original architecture (Carr & Ollis, 2009; Ollis *et al.*, 1992). It is therefore possible that the cap domain in hHSL is composed entirely of this region because hHSL does not contain a region corresponding to the other parts of the cap region of Est25 (amino-acid residues 1–85 including the $\alpha1$ and $\alpha2$ helices). In this context, we hypothesized that the regulatory module of hHSL exerts a function similar to that of the cap region of Est25 in the control of catalytic activity and substrate specificity; this model is supported by mutation analysis of the regulatory module of hHSL (Wang *et al.*, 2005)

The catalytic activity of most enzymes that possess an α/β-hydrolase fold depends primarily on a highly conserved catalytic triad of Ser, His and Asp/Glu residues. In Est25, the catalytic Ser201 was located between $\beta5$ and $\alpha5$, while the other two residues (Asp303 and His333) were found between $\beta7$ and $\alpha9$ and between $\beta8$ and $\alpha10$, respectively (Fig. 4*c*). Using site-directed mutagenesis, Ser201 was confirmed to be the catalytic residue in Est25 (Kim *et al.*, 2006). Consistent with other α/β-hydrolases, Ser201 was situated in the apex of the nucleophilic elbow between strand $\beta5$ and helix $\alpha5$ and its backbone angles were in the disallowed region of the Ramachandran plot (φ = 63° and ψ = −121°). The three amino acids in the catalytic triad were located in close proximity and had a highly specific configuration (Fig. 4*a*). The hydrogen-bond distances within the catalytic triad were 2.7 Å from Ser201 O^{γ} to His333 $N^{\varepsilon2}$ and 2.6 Å from His333 $N^{\delta1}$ to Asp303 $O^{\delta2}$. In addition, the formation of the oxyanion hole of Est25 was likely to be mediated by Gly125, Gly126 and Gly202. Gly125 and Gly126 were located in the ^{124}HGGG^{127} sequence motif located approximately 80 amino-acid residues upstream of the active-site Ser201. Gly202 was fixed by hydrogen bonds between its amino group and the OG1 atom of Ser201 (3.0 Å) and between the carbonyl group and the ND1 atom of Leu206 (3.0 Å). The O atom of Gly126 was linked to the N atoms of Val129 and

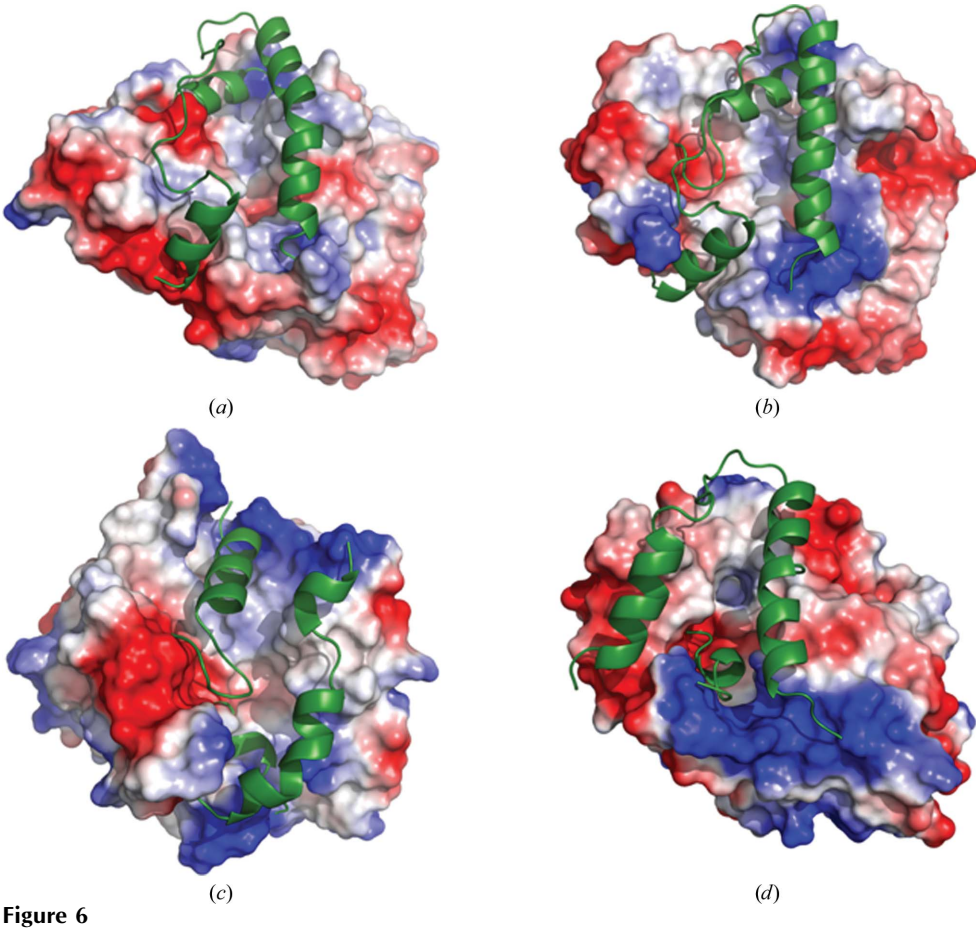

Figure 6
Electrostatic potential representations of Est25 and three structurally homologous enzymes. The electrostatic potentials of the negatively charged (red) and positively charged (blue) regions are shown. The cap regions above the substrate-binding pocket are shown as ribbon diagrams (green). Note that the cap-domain helices surround the substrate-binding pocket. (*a*) Est25, (*b*) BFAE, (*c*) AFEST, (*d*) PestE. All structures are aligned in the same orientation based on the active-site residues.

Ile130, while the N atom of Gly125 made hydrogen bonds to the O atoms of Glu200 and Tyr138. Sequence motifs that are involved in catalysis, such as ^{124}HGGG^{127}, ^{199}G*X*S*X*GGNL^{206} and ^{303}DP*XX*D^{307}, are common to HSL-family members and Est25, indicating that these enzymes share the same catalytic mechanism.

3.4. Structural comparison with other proteins

A search using the *DALI* server identified several proteins with significant structural homology to Est25 (Holm & Rosenström, 2010). The structure of Est25 was most similar to that of brefeldin A esterase (BFAE) from *B. subtilis* (PDB entry 1jkm; Wei *et al.*, 1999), with a *Z*-score of 55.3. After structure-based superposition, the r.m.s.d. for C^{α} atoms between the two structures was 1.47 Å for 344 residues. BFAE hydrolyzes and inactivates a potent fungal inhibitor of secretory transport. In addition, a hyperthermophilic carboxylesterase (AFEST) from *A. fulgidus* (PDB entry 1jji, *Z*-score = 39.4, r.m.s.d. = 3.19 Å for 304 residues; De Simone *et al.*, 2001) and a highly thermostable esterase (PestE) from *P. calidifontis* VA1 (PDB entry 3zwq, *Z*-score = 40.6, r.m.s.d. = 2.56 Å for 304 residues; Palm *et al.*, 2011) showed structural similarity to Est25. These three enzymes (BFAE, AFEST and PestE) are 24.6–46.5% identical in primary sequence to Est25, with 60 residues being completely conserved among all four enzymes (Fig. 5, upper part). The core residues of the α/β-hydrolase fold as well as residues important for catalysis are highly conserved in these proteins. For example, the ^{124}HGGG^{127} motif of Est25 superimposed well with those of BFAE (r.m.s.d. of 0.143 Å for all atoms), AFEST (r.m.s.d. of 0.276 Å for all atoms) and PestE (r.m.s.d. of 0.309 Å for all atoms). Large overlaps in ^{199}G*X*S*X*GGNL^{206} and ^{303}DPLRDEG^{309} were also observed in these proteins (Fig. 5, lower part).

However, the alignment and orientation of α-helices in the cap domain showed an intriguing structural variation among these proteins. The cap domain of Est25 can be described as having a horseshoe-shaped entrance consisting of three distinct helices. However, the cap domains of other structural homologues have different topologies and the amino-acid residues in the cap domain were not well aligned among these proteins (Fig. 6). These helices in the cap domain were amphipathic and most of the hydrophobic residues (Tyr60, Trp68, Phe72, Leu255 and Tyr267) in the cap domain of Est25 were buried and located over the active site. Furthermore, the *B* factors for the cap domain were 19.8 Å^2 (main chain) and 22.7 Å^2 (side chains), which are high compared with those of the overall structure of Est25 (main-chain atoms, 14.3 Å^2; side-chain atoms, 15.3 Å^2). The substrate-binding pocket of Est25 had a deep and narrow gorge which extended approximately 17 Å from the protein surface to the catalytic Ser201 residue. The catalytic residues were buried at the bottom of a binding pocket which protects the active site from exposure to water. At the entrance of the binding pocket, Tyr60 and Trp68 in the α2 helix, together with Asp256 in the loop between the α6 and α7 helices on the opposite side, may facilitate substrate entry by hydrophobic and electrostatic interactions. Large hydrophobic regions were formed in the middle of the substrate-binding pocket by the side chains of Phe72, Ile130, Tyr232, Phe254, Leu255 and Met260. The main-chain atoms of the loop regions as well as the catalytic residues (Ser201, His333 and Asp303) were located in the bottom of the binding pocket. Only two acidic residues were found in the binding pocket: Asp256 at the entrance and Glu200 near the base.

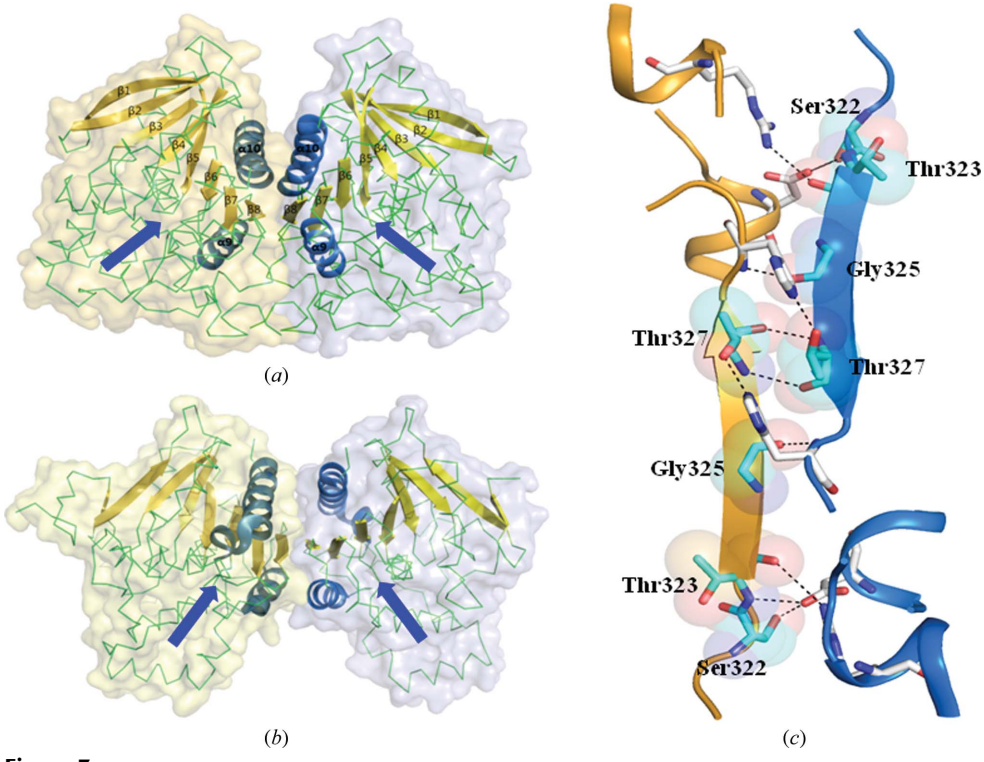

Figure 7
Representation of the dimeric interface in Est25. The dimeric organizations of Est25 (*a*) and hMGL (*b*) are shown. The molecular surfaces of the two subunits in a dimer are shown in light yellow (left) and light blue (right), respectively. The continuous strands are shown in dark yellow. The two interfacing helices are shown in dark blue. (*c*) A hydrogen-bond network between two β8 strands of each Est25 subunit (yellow and green, respectively) is shown in stick representation.

3.5. Dimeric interface

The four molecules in the asymmetric unit of Est25 were arranged as a dimer of dimers. An interesting feature of the Est25 dimer was that the core β-sheets of each monomer were related by twofold symmetry to form an

extended intermolecular 16-stranded β-sheet (Fig. 7). The dimer was formed by edge-to-edge interactions of the two monomers, and the catalytic triad was relatively distant from the dimer interface. In accordance, three enzymes homologous to Est25 (BFAE, AFEST and PestE) are reported to form dimers in solution and their dimeric interfaces exhibited strong similarities to that of Est25 (data not shown). The area of the dimer interface of Est25 (1165 Å^2) was smaller than those of BFAE (1391 Å^2), AFEST (1511 Å^2) and PestE (1354 Å^2) but larger than that of hMGL (853 Å^2). The dimer interface was formed mainly by helices α9 and α10 and the β8/α10 loop, which includes a salt bridge between Arg314 (on the α9 helix) and Glu301 (on the loop between the β7 strand and the α9 helix). 14 hydrogen bonds were formed involving the residues Ser322, Thr323, Gly325, Thr327, His329 and Asp345 of each monomer (Fig. 7*c*). In addition, Tyr313, Leu317, Val324, Arg352 and Phe357 were the residues mainly involved in nonpolar contacts at the dimeric interface.

Dimerization is essential for the catalytic activity and the thermostability of the HSL family of enzymes (Byun *et al.*, 2007; Shen *et al.*, 2000). Accordingly, the hyperthermostability of Est25 is most likely to arise from strong hydrophobic interactions at the dimeric interface (Kim *et al.*, 2006). The requirement of dimerization for the function and stability of HSL-family enzymes focuses attention on the dimeric interface as a potential target for structure-aided drug design. Notably, disruption of dimerization has successfully been employed as a strategy for the development of effective inhibitors (Petch *et al.*, 2012; Zhao *et al.*, 2010).

3.6. Cross-linked enzyme aggregates (CLEAs) of Est25

Immobilized enzymes serve as highly efficient and specific catalysts for the preparation of pharmaceutical compounds (Brady & Jordaan, 2009; Hanefeld *et al.*, 2009). To investigate the effect of immobilizing Est25 on enzyme performance, CLEAs (CLEA-Est25) were prepared by precipitating the enzyme with ammonium sulfate followed by glutaraldehyde cross-linking. Scanning electron-microscopic images of CLEA-Est25 showed large globular structures with high

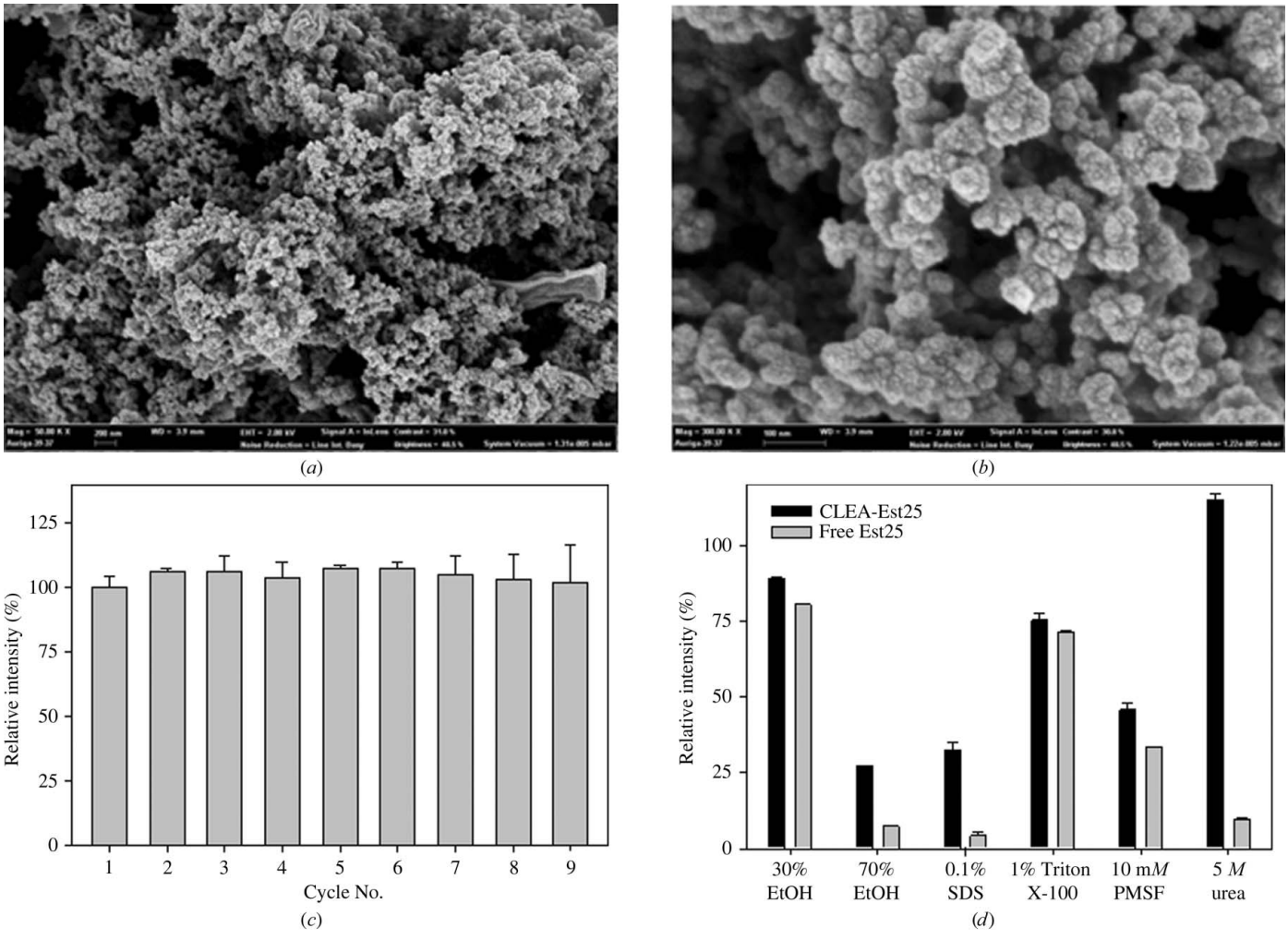

Figure 8
Cross-linked enzyme aggregates (CLEAs) of Est25. Field emission scanning electron microscopic (FE-SEM) images of CLEA-Est25 at magnification ratios of 50 000 (*a*) and 300 000 (*b*) are shown. (*c*) The stability of CLEA-Est25 activity was investigated through nine cycles of reuse. (*d*) The chemical stabilities of CLEA-Est25 and free soluble Est25 were compared by measuring residual activities after 1 h incubations with various chemical compounds.

surface density (Figs. 8*a* and 8*b*). CLEA-Est25 could be reused for nine assay cycles without significant activity loss (Fig. 8*c*), indicating a degree of stability essential for repetitive use as an industrial biocatalyst. The effects of various chemical compounds on the activities of CLEA-Est25 and free Est25 were examined by measuring the residual activity after 1 h incubations. The enzymatic activity of CLEA-Est25 in the presence of EtOH, SDS, Triton X-100, PMSF and urea underscored the effect of enzyme immobilization. Specifically, in the presence of 0.1%(*v*/*v*) SDS or 70% EtOH free Est25 lost almost all of its initial activity within 1 h, while CLEA-Est25 retained 30–40% of its initial activity (Fig. 8*d*). Although incubation with 5 *M* urea almost completely inactivated free Est25, the residual activity of CLEA-Est25 under the same conditions was very similar to or even higher than the original Est25 activity. Therefore, CLEA-Est25 may potentially be effectively used as a biocatalyst under various nonphysiological conditions. Accordingly, hydrolases, lipases and oxidases immobilized as cross-linked aggregates (CLEAs) are under investigation for use as stable biocatalysts (Ju *et al.*, 2013; Kartal & Kilinc, 2012; Taboada-Puig *et al.*, 2011).

4. Conclusion

In this study, the structure of Est25, a bacterial homologue of HSL from a metagenomic library, was determined at 1.49 Å resolution. In addition, its catalytic properties as well as its immobilization abilities were investigated. The structural determination and biochemical characterization of Est25 presented here allowed us to deduce the structural and functional roles of the cap domain, binding pockets and dimeric interfaces, as well as the overall fold of Est25. The current results further provide a clue for the development of new HSL inhibitors, because Est25 and HSL share the essential motifs for catalysis. Immobilization of Est25 significantly increased the stability of the enzyme in various deactivating conditions, indicating the potential for the repetitive use of cross-linked enzyme aggregates as biocatalysts in industrial applications.

This work was supported by a National Research Foundation Grant (2012R1A1A2000910) funded by the Korean Government to TDK. KKK is supported by the Next-Generation BioGreen 21 Program (SSAC PJ008107), Korea Healthcare Technology R&D Project (A092006) and the National Research Foundation of Korea (NRF; grant 2011-0028878).

References

Adams, P. D. *et al.* (2010). *Acta Cryst.* D**66**, 213–221.
Angkawidjaja, C., Koga, Y., Takano, K. & Kanaya, S. (2012). *FEBS J.* **279**, 3071–3084.
Arpigny, J. L. & Jaeger, K.-E. (1999). *Biochem. J.* **343**, 177–183.
Brady, D. & Jordaan, J. (2009). *Biotechnol. Lett.* **31**, 1639–1650.
Byun, J.-S., Rhee, J.-K., Kim, N. D., Yoon, J., Kim, D.-U., Koh, E., Oh, J.-W. & Cho, H.-S. (2007). *BMC Struct. Biol.* **7**, 47.
Carr, P. D. & Ollis, D. L. (2009). *Protein Pept. Lett.* **16**, 1137–1148.
Cascio, G., Schiera, G. & Di Liegro, I. (2012). *Curr. Diabetes Rev.* **8**, 2–17.
Chayen, N. E., Shaw Stewart, P. D., Maeder, D. L. & Blow, D. M. (1990). *J. Appl. Cryst.* **23**, 297–302.
Chronopoulou, E. G. & Labrou, N. E. (2009). *Recent Pat. Biotechnol.* **3**, 211–223.
De Simone, G., Galdiero, S., Manco, G., Lang, D., Rossi, M. & Pedone, C. (2000). *J. Mol. Biol.* **303**, 761–771.
De Simone, G., Menchise, V., Manco, G., Mandrich, L., Sorrentino, N., Lang, D., Rossi, M. & Pedone, C. (2001). *J. Mol. Biol.* **314**, 507–518.
Emsley, P. & Cowtan, K. (2004). *Acta Cryst.* D**60**, 2126–2132.
Gouet, P., Robert, X. & Courcelle, E. (2003). *Nucleic Acids Res.* **31**, 3320–3323.
Hanefeld, U., Gardossi, L. & Magner, E. (2009). *Chem. Soc. Rev.* **38**, 453–468.
Herter, S., Nguyen, G. S., Thompson, M. L., Steffen-Munsberg, F., Schauer, F., Bornscheuer, U. T. & Kourist, R. (2011). *Appl. Microbiol. Biotechnol.* **90**, 929–939.
Holm, C. (2003). *Biochem. Soc. Trans.* **31**, 1120–1124.
Holm, L. & Rosenström, P. (2010). *Nucleic Acids Res.* **38**, W545–W549.
Hwang, H., Kim, S., Yoon, S., Ryu, Y., Lee, S. Y. & Kim, T. D. (2010). *Int. J. Biol. Macromol.* **46**, 145–152.
Jones, D. T. & Swindells, M. B. (2002). *Trends Biochem. Sci.* **27**, 161–164.
Ju, H., Jang, E., Ryu, B. H. & Kim, T. D. (2013). *Bioresour. Technol.* **128**, 81–86.
Karpe, F., Dickmann, J. R. & Frayn, K. N. (2011). *Diabetes*, **60**, 2441–2449.
Kartal, F. & Kilinc, A. (2012). *Biotechnol. Prog.* **28**, 937–945.
Kim, S., Bae, S. Y., Kim, S. J., Ngo, T. D., Kim, K. K. & Kim, T. D. (2012). *Int. J. Biol. Macromol.* **50**, 103–111.
Kim, Y.-J., Choi, G.-S., Kim, S.-B., Yoon, G.-S., Kim, Y.-S. & Ryu, Y.-W. (2006). *Protein Expr. Purif.* **45**, 315–323.
Kim, S., Joo, S., Yoon, H. C., Ryu, Y., Kim, K. K. & Kim, T. D. (2007). *Acta Cryst.* F**63**, 579–581.
Lafontan, M. & Langin, D. (2009). *Prog. Lipid Res.* **48**, 275–297.
Langer, G., Cohen, S. X., Lamzin, V. S. & Perrakis, A. (2008). *Nature Protoc.* **3**, 1171–1179.
Laskowski, R. A., MacArthur, M. W., Moss, D. S. & Thornton, J. M. (1993). *J. Appl. Cryst.* **26**, 283–291.
Manco, G., Merone, L., Porzio, E., Feng, Y. & Mandrich, L. (2012). *Protein Pept. Lett.* **19**, 144–154.
Murshudov, G. N., Skubák, P., Lebedev, A. A., Pannu, N. S., Steiner, R. A., Nicholls, R. A., Winn, M. D., Long, F. & Vagin, A. A. (2011). *Acta Cryst.* D**67**, 355–367.
Nam, K. H., Kim, M.-Y., Kim, S.-J., Priyadarshi, A., Kwon, S.-T., Koo, B.-S., Yoon, S.-H. & Hwang, K. Y. (2009). *Proteins*, **74**, 1036–1040.
Ollis, D. L., Cheah, E., Cygler, M., Dijkstra, B., Frolow, F., Franken, S. M., Harel, M., Remington, S. J., Silman, I., Schrag, J., Sussman, J. L., Verschueren, K. H. G. & Goldman, A. (1992). *Protein Eng.* **5**, 197–211.
Osterlund, T. (2001). *Eur. J. Biochem.* **268**, 1899–1907.
Otwinowski, Z. & Minor, W. (1997). *Methods Enzymol.* **276**, 307–326.
Palm, G. J., Fernández-Álvaro, E., Bogdanović, X., Bartsch, S., Sczodrok, J., Singh, R. K., Böttcher, D., Atomi, H., Bornscheuer, U. T. & Hinrichs, W. (2011). *Appl. Microbiol. Biotechnol.* **91**, 1061–1072.
Petch, D., Anderson, R. J., Cunningham, A., George, S. E., Hibbs, D. E., Liu, R., Mackay, S. P., Paul, A., Small, D. A. & Groundwater, P. W. (2012). *Bioorg. Med. Chem.* **20**, 5901–5914.
Podust, L. M. & Sherman, D. H. (2012). *Nat. Prod. Rep.* **29**, 1251–1266.
Rehdorf, J., Behrens, G. A., Nguyen, G. S., Kourist, R. & Bornscheuer, U. T. (2012). *Appl. Microbiol. Biotechnol.* **93**, 1119–1126.
Rodriguez, J. A., Ben Ali, Y., Abdelkafi, S., Mendoza, L. D., Leclaire, J., Fotiadu, F., Buono, G., Carrière, F. & Abousalham, A. (2010). *Biochim. Biophys. Acta*, **1801**, 77–83.
Shen, W. J., Patel, S., Hong, R. & Kraemer, F. B. (2000). *Biochemistry*, **39**, 2392–2398.

Sievers, F., Wilm, A., Dineen, D., Gibson, T. J., Karplus, K., Li, W., Lopez, R., McWilliam, H., Remmert, M., Söding, J., Thompson, J. D. & Higgins, D. G. (2011). *Mol. Syst. Biol.* **7**, 539.
Taboada-Puig, R., Junghanns, C., Demarche, P., Moreira, M. T., Feijoo, G., Lema, J. M. & Agathos, S. N. (2011). *Bioresour. Technol.* **102**, 6593–6599.
Tamura, K., Peterson, D., Peterson, N., Stecher, G., Nei, M. & Kumar, S. (2011). *Mol. Biol. Evol.* **28**, 2731–2739.
Terwilliger, T. C. (2001). *Acta Cryst.* D**57**, 1763–1775.
Terwilliger, T. C. & Berendzen, J. (1999). *Acta Cryst.* D**55**, 1872–1877.
Vagin, A. & Teplyakov, A. (2010). *Acta Cryst.* D**66**, 22–25.
Wang, J., Shen, W.-J., Patel, S., Harada, K. & Kraemer, F. B. (2005). *Biochemistry*, **44**, 1953–1959.
Wei, Y., Contreras, J. A., Sheffield, P., Osterlund, T., Derewenda, U., Kneusel, R. E., Matern, U., Holm, C. & Derewenda, Z. S. (1999). *Nature Struct. Biol.* **6**, 340–345.
Zhao, T. T., Le Francois, B. G., Goss, G., Ding, K., Bradbury, P. A. & Dimitroulakos, J. (2010). *Oncogene*, **29**, 4682–4692.
Zhu, X., Larsen, N. A., Basran, A., Bruce, N. C. & Wilson, I. A. (2003). *J. Biol. Chem.* **278**, 2008–2014.